FULL PAPER

Applied Organometallic Chemistry **WILEY**

New solvatochromic complexes of 1,2-bis[(5,6-diphenyl-1,2,4-triazin3-yl)hydrazinylidene-methyl]benzene: Synthesis, spectroscopic, biological, docking, and theoretical studies

Fatma Samy ⓘ | Ali Taha ⓘ | Fouz M. Omar ⓘ

Department of Chemistry, Faculty of Education, Ain Shams University, Cairo, Egypt

Correspondence
Fatma Samy, Department of Chemistry, Faculty of Education, Ain Shams University, Roxy, Cairo 11341, Egypt.
Email: fatma_chem2000@yahoo.com; fatmasame@edu.asu.edu.eg

A new bistriazine hydrazone ligand (H_2L; H_2BDTB) is derived from 5,6-diphenyl-1,2,4-triazine-3-ylhydrazine (DTH) with o-phthalaldehyde in ratio (2:1). The Fe(III), Co(II), Ni(II), Cu(II), and Th(IV) complexes (**1–5**), as well as the Co(II) complex (**6**) (prepared in the presence of cetyltrimethylammonium bromide [CTAB]), are synthesized. They are characterized by elemental analyses, spectral (ultraviolet–visible [UV–Vis], infrared [IR], mass, ^1H NMR, and electron spin resonance [ESR]), magnetic susceptibility, molar conductivity, and thermal gravimetric analysis (TGA) measurements; and morphological structures are scanned by electron microscopy (SEM) that showed rod shape, irregular bulk sheets, and fused aggregated clusters for free ligand, Co(II) complexes (**2** and **6**), respectively. Moreover, cobalt(II) complex (**6**) exhibited an octahedral geometry; however, cobalt(II) complex (**2**) showed square planar geometry as deduced from magnetic moment and UV–Vis measurements. Fluorescence spectra for ligand and its Fe(III) and Th(IV) complexes have been measured in different solvents to investigate their solvatochromic behavior that used to estimate dipole moments either in ground and excited states. The antimicrobial and antitumor activities of free ligand and its complexes were investigated, in addition to molecular docking studies using MOE 2014.0901 software (PDB. I.D.3ce3). The data showed that Co(II) complex (**6**) can be nominated as one of the most powerful antitumor. The theoretical calculation for bistriazine ligand and its complexes were performed using DFT and *PM3*, and the data are correlated with the experimental results.

KEYWORDS
(DFT & *PM3*) molecular modeling, bis-triazine complexes, fluorescence spectra, ground and excited state, solvatochromic

1 | INTRODUCTION

Hydrazones and their metal complexes show a vital role in frequent fields such as biomedical, wastewater remediation,[1] optoelectronic,[2] analytical,[3] photoresponse,[4] catalytic,[5] and cytotoxicity[6] studies. They used also as anticancer,[7] antihypertensive,[8] antitubercular,[9] antiproliferative,[10] antitumor,[11–13] antioxidant,[14] and chemotherapeutic agents.[15]

The bistriazine compounds are important, as they have two triazine rings in addition to many phenyl rings that extended the conjugation system. So, they are used in many fields such as a fluorescent brightener,[16] optoelectronic properties,[17] and luminescent blue emitters.[18] Furthermore, they have many applications such as antimicrobial and anticancer activities.[11,19–22]

Numerous methods for describing solvatochromism in terms of solvent characteristics based on the Onsager description of nonspecific electrostatic solute–solvent interactions have been proposed to estimate the ground and excited state dipole moments.[21–29]

This work is an extension of our work on 5,6-diphenyl-1,2,4-triazine-3-ylhydrazine (DTH) as a starting material.[4a,11a,b,30,31,32–36] The aim of this work deals with the synthesis of new complexes of hydrazone (H$_2$BDTB) and 1,2-bis[(5,6-diphenyl-1,2,4-triazin3-yl)hydrazinylidenemethyl]benzene that allowed to coordinate with Co(II), Ni(II), Cu(II), Fe(III), and Th(IV) metal ions. They are characterized by different spectroscopic techniques, as well as thermal gravimetric analysis (TGA) and magnetic moment and molar conductance measurements. The ground (μ_g) and excited (μ_e) state dipole moments have been calculated by using solvatochromic methods. Antimicrobial studies of the ligand and its metal complexes are screened against selected kinds of two pathogenic Gram-negative and two Gram-positive pathogenic bacteria, yeasts, and fungi strain. The antitumor activity of the hydrazone ligand and its complexes was investigated against hepatocellular carcinoma cells (Hep G-2). Molecular docking using MOE 2014.0901 software (PDB. I.D.3ce3) and theoretical calculations of free ligand and its complexes were carried out at 6-31G and *PM3* levels implemented at *Hyperchem* 7.52 and Gaussian 09 programs.

2 | EXPERIMENTAL

2.1 | Materials and methods

Metal salts, thiosemicarbazide, benzil, glacial acetic acid, lithium hydroxide, hydrazine hydrate (100%), o-phthalaldehyde, and cetyltrimethylammonium bromide (CTAB) were either BDH, Aldrich, or Merck products. The organic solvents were reagent-grade chemicals and used without further purification.

2.2 | Measurements

The percent of C, N, and H was determined using Vario El-Elementar at the Ministry of Egypt Defense, Chemical War Department. Analyses of the metal content were followed by the dissolution of the solid complex in concentrated HNO$_3$ acid and were determined complexometrically using 0.001-M EDTA solution.[37] Stuart melting point instrument was used to record decomposition temperatures. Infrared (IR) and electronic spectra were measured using the Nicolet 6700 FT-IR spectrometer and the Jasco model V-550 ultraviolet–visible (UV–Vis) spectrophotometer, respectively. ^{1}H NMR and mass spectra were measured on Bruker WP 200 SY and Shimadzu QP-2010 Plus gas chromatography GCMSqp 1000 ex Bruker WP 200 SY mass spectrometers. However, electron spin resonance (ESR) spectra measured using an Elexsys E500, Bruker. The magnetic susceptibility was determined using magnetic susceptibility balance of the type Johnson Matthey (Alfa product, Model No. MKI), and the molar susceptibility was corrected using Pascal's constants for the diamagnetism of all atoms in the compounds.[38] The molar conductivities and TG analysis were measured using the Corning conductivity meter NY 14831 model 441 and a Shimadzu-50 instrument, respectively. The morphology structure of the present compounds was distinguished by using the scanning electron microscopy (SEM) apparatus, FEI, Netherlands, Model Quanta 250 FEG. The PerkinElmer LS 55 Luminescence spectrometer (USA) was used to measure the fluorescence spectra of the current compounds.

2.3 | Synthesis of the ligand, H$_2$BDTB

The hydrazinotriazine DTH was prepared according to the method reported in the literature.[36] The ethanolic solution of DTH was added to the acidified solution of o-phthalaldehyde in a molar ratio (2:1). The mixture was heated under reflux for 2 h. The yellowish precipitated was filtered off and washed by hot ethanol; the dried product (H$_2$BDTB) has m.p. 195°C with yield 90% and stored in an evacuated desiccator over anhydrous calcium chloride.

2.4 | Synthesis of the bistriazine complexes

The ethanolic solution of the ligand H_2BDTB was heated under reflux with an aqueous LiOH solution for ½ h, and then the metal ion solution was added gradually to the mixture, in molar ratio 1:2:2 (ligand: LiOH:M). Similar method used to synthesize Co(II) complex (**6**) but by adding CTAB to the mixture. The mixture was heated under reflux for 6–8 h, and the colored precipitates were filtered off and washed with water, then with EtOH, and finally with diethyl ether. The new complexes (**1–6**) are stored in desiccator over anhydrous calcium chloride.

2.5 | Biological studies

The antimicrobial and antitumor activities of H_2BDTB and its metal complexes against Gram-positive (*Staphylococcus aureus* [ATCC 25923] and *Bacillus subtilis* [ATCC 6635]) and Gram-negative (*Salmonella typhimurium* [ATCC 14028] and *Escherichia coli* [ATCC 25922]) bacteria, yeasts and fungi (*Candida albicans* [ATCC 10231] and *Aspergillus fumigatus*), and hepatocellular carcinoma cells (Hep G-2) were performed using the technique reported in the literature.[39–41] Chloramphenicol, cephalothin, and cycloheximide drugs are used as references for Gram-positive, Gram-negative bacteria, and fungi, respectively.

2.6 | Molecular docking

MOE was preferred for docking among various available resources as it is adaptable, has available source code, gives binding affinity score, shows interacting amino acids with position, and is user-friendly. It is also represents a good graphical view of results by showing ligand and receptor binding residues with their positions and interactions. In MOE2014.0901 software (PDB. I.D.3ce3), receptor–ligand binding affinities with all feasible binding geometries are precedence on the basis of a numerical value called S-score. MOE identifies salt bridges, hydrogen bonds, and hydrophobic interactions and gives the S-score. Interactions of inhibitors with receptor proteins are predicted on the basis of the S-score within the active site of the crystallized structure.[42]

The X-ray crystallographic structure of c-Met kinase (PDB. ID: 3ce3) at 1.85-Å resolution was retrieved from the protein data bank.[43] The used protein was prepared for the docking study using *Protonate 3D* protocol in MOE with default options. Triangle Matcher placement method and London dG scoring function were used for docking. The active sites are defined by all the amino acid residues involved in the interaction with the co-crystallized ligand (inhibitors).

## 2.7 | Molecular orbital calculations

The optimized structures of ligand (H_2BDTB) and its complexes (**1–4** and **6**) were determined at semiempirical (*PM3*) level using *Hyperchem 7.52* program,[44] and density functional theory (DFT) calculations at basis set (6-31G) were performed on the ligand and its cobalt (II) complex (**2**) using Gaussian 09 program package.[45]

3 | RESULTS AND DISCUSSION

3.1 | Characterization of the bistriazine ligand

The ligand H_2BDTB has two tautomeric forms represented in Scheme 1, H_2L^a is the most favorable form according to their gap energy calculated using *PM3*, Egap 7.887 and 6.130 eV for H_2L^a and H_2L^b, respectively. The structure of this ligand is characterized on the basis of C, H, and N analysis, IR, UV–Vis, ^1HNMR, and mass spectral techniques data that collected in Tables 1–3.

The IR spectrum of H_2BDTB showed the stretching vibrations modes at 1588, 1521, 1457, and 1228 cm^{-1} (Table 2) those assigned for $C=N_{Azomethine}$, $C=N_{Triazine}$, $N=N_{Triazine}$, and N–N groups, respectively.[11,30,32,33] However, the bands observed in the UV–Vis spectrum of H_2BDTB in DMF solution at 280 and 336 nm (Table 3) refer to $\pi–\pi^*$ and $n–\pi^*$ transitions.[30,31,46] Additionally, the ^1HNMR spectrum of the ligand exhibited chemical shifts (δ/ppm) at 7.25–7.65 (24 H, phenyl groups, m), 8.19 (2H, CH=N, s),[47] and 9.29 (2H, NH of hydrazino, s).[48] The downfield shift of $NH_{hydrazino}$ in H_2BDTB spectrum suggests the formation of intramolecular hydrogen bonding with the $N_{azomethine}$[49] that disappeared on deuteration.[50] Furthermore, the molecular ion peak of the H_2BDTB in
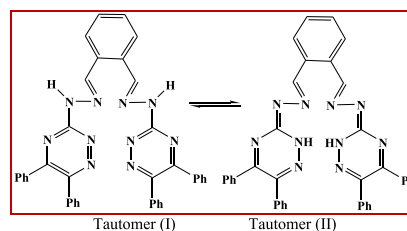
SCHEME 1 Tautomeric forms of the H_2BDTB

TABLE 1 Analytical and physical data of H$_2$BDTB compounds

No.	Reaction	Complex [F. Wt]	Color	Yield (%)	MP °C	Elemental analysis, % found/(calc.)			
						C	H	N	M
		Ligand [624.71]	Yellow	90	195	72.71 (73.06)	4.77 (4.52)	22.04 (22.42)	--------
1	H$_2$L + Fe (NO$_3$)$_3$	[FeL (EtOH)$_2$]NO$_3$.½H$_2$O [841.69]	Black crystals	69	225[b]	60.19 (59.93)	4.91 (4.67)	18.61 (18.31)	6.31 (6.64)
2	H$_2$L + Co (NO$_3$)$_2$	[CoHL(H$_2$O)EtOH]NO$_3$ [808.72]	Deep green	67	>300	59.80 (59.41)	4.09 (4.36)	19.46 (19.05)	7.02 (7.29)
3	H$_2$L + Ni (NO$_3$)$_2$	[NiHL(H$_2$O)$_2$]NO$_3$.H$_2$O [798.46]	Brown	65	>300	57.27 (57.16)	3.86 (4.17)	19.10 (19.30)	7.26 (7.35)
4	H$_2$L + Cu (NO$_3$)$_2$	[CuH$_2$L(H$_2$O)$_3$(NO$_3$)]NO$_3$.H$_2$O[884.32]	Black	75	280[b]	51.43 (51.61)	3.64 (4.10)	19.09 (19.01)	7.11 (7.19)
5	H$_2$L + Th (NO$_3$)$_4$	[Th$_2$H$_2$L(H$_2$O)$_4$(NO$_3$)$_8$] [1656.88]	Green	26	>300	27.66 (27.55)	1.86 (2.19)	15.05 (15.22)	[a] (28.01)
6	H$_2$L + Co (NO$_3$)$_2$ + CTAB	[CoL(H$_2$O)$_2$].1½EtOH [786.76]	Deep green	70	>300	62.84 (62.59)	4.53 (5.00)	17.72 (17.80)	7.23 (7.49)

[a]Not determined.
[b]Shrinking.

TABLE 2 Characteristic IR spectral data of H$_2$BDTB and its complexes

No.	IR spectra (cm)$^{-1}$					
	ν (NH) and/or ν (OH)	Coord. ν(C=N) azomethine	Coord ν(C=N) triazine	ν(M–O)	ν(M–N)	Other bands
H$_2$L	3287, 3207	1588	1521	—	—	
1	3430	1562	1498	545	450	1470; ν (NO$_3^-$) ionic nitrate
2	3384	1579	1498	544	462	1458; ν (NO$_3^-$) ionic nitrate
3	3379	1582	1497	542	466	1465; ν (NO$_3^-$) ionic nitrate
4	3430	1582	1510	540	454	1468; ν (NO$_3^-$) ionic nitrate 1374; ν (NO$_3^-$) monodentate nitrate
5	3424	1564	1516	544	486	1388; ν (NO$_3^-$) monodentate nitrate
6	3375	1570	1515	537	450	

the mass spectrum appeared at 624.08, which is consistent with the formula mass (624.08) proposed by elemental analysis. Figure 1 showed that the morphological structure of the H$_2$BDTB, recorded by scanning electron microscope, indicates a rod shape.

3.2 | Characterization of the bistriazine complexes

The new bistriazine complexes were characterized by using physical and spectroscopic techniques; their elemental analysis data and physical properties are summarized in Table 1. All complexes are colored, thermally stable, and sparingly soluble in water and common organic solvents but partially soluble in dimethyl sulfoxide (DMSO) and dimethyl formamide (DMF). Scheme 2 depicts the plausible structures of the present complexes.

3.2.1 | IR spectra and conductivity measurements

Table 2 collects the main IR bands with their tentative assignments; the stretching vibrations appeared in the range of 3375–3430 cm^{-1} may be assigned to NH and/or

TABLE 3 Electronic spectra, magnetic moments, and molar conductivity data of H₂BDTB and its complexes

No.	μ_{eff} BM	Conductance[a] (Ω^{-1} cm² mol⁻¹)	Electronic spectral bands[b] λ_{max} (nm) (DMF) [Nujol mull][c]
H₂L	----	-----	(336, 280)
1	1.32	63	(525)[548][c]
2	2.46	61	(434)[593][c]
3	3.89	84	(396)[499][c]
4	2.14	60	[595][c]
5	Diamagnetic	11	[333][c]
6	4.84	13	(539)

[a]Solutions in DMF (10^{-3} M).
[b]Concentrated solutions.
[c]Nujol mull.
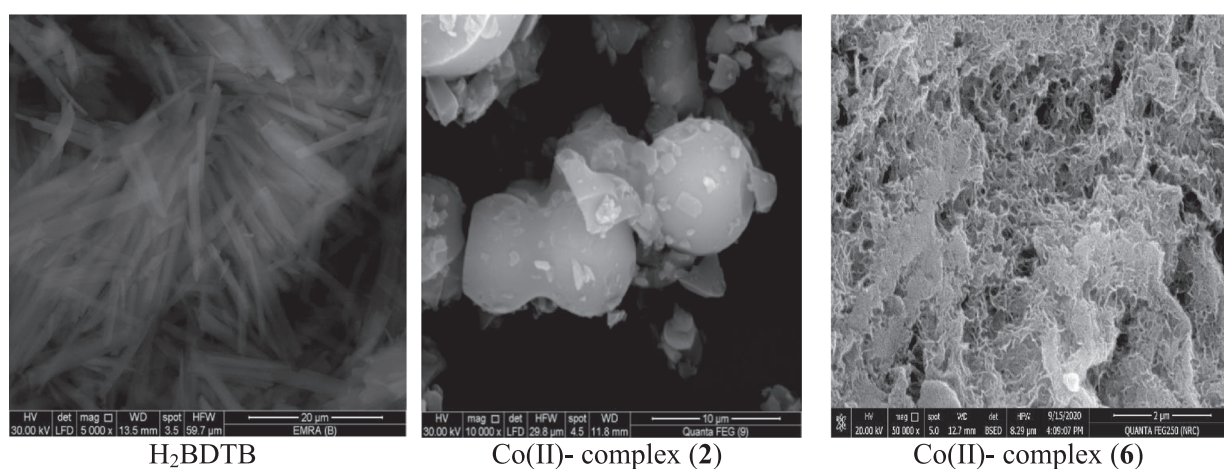
FIGURE 1 SEM of the H₂BDTB and Co(II) complexes (**2** and **6**)

OH groups.[51–57] The ν(C=N)azomethine of the ligand (H₂BDTB) observed at 1588 cm⁻¹ exhibits a shift to a lower frequency in the range of 1562–1582 cm⁻¹ in complexes.[30,31] Additionally, ν(C=N)triazine of the H₂BDTB observed at 1521 cm⁻¹ shifted in complexes to the range 1497–1516 cm⁻¹, suggesting allocation of C=N$_{azomethine}$ and C=N$_{triazine}$ as coordination centers.[9,30,31,32] IR spectra of Cu(II) and Th(IV) complexes (**4** and **5**) showed new bands at 1374 and 1388 cm⁻¹, respectively, which may be due to coordinated nitrate group.[58–60] However, the complexes (**1–4**) have bands in the range of 1458–1470 cm⁻¹, proposing ionic nature of nitrate.[61] The new bands observed in the ranges 537–545 and 450–486 cm⁻¹ are attributed to M–O and M–N bonds, respectively.[11,61,62]

The conductance measurements (Table 3) confirmed that all complexes are electrolytic (1:1), because they have conductance values in the range 60–84 Ω^{-1} cm² mol⁻¹. However, complexes (**5** and **6**) showed values 11 and 13 Ω^{-1} cm² mol⁻¹, proposing non-electrolytic complexes; this finding agrees with IR data.[63]

3.2.2 | UV–Vis spectra and magnetic measurements

The low magnetic moment (Table 3) measured for Fe(III) complex (**1**) (1.32 BM), compared with that reported (2.1–2.5 BM) for low-spin octahedral geometry ($t_{2g}^5\ e_g^0$), might attributed to the antiferromagnetic interactions of Fe(III) ions with those found in their neighboring molecules in the crystal lattice.[64] But the magnetic moment value of the Cu(II) complex (**4**) is 2.14, which is expected for d¹ configuration of Cu(II) complex.[65] On the other hand, the magnetic moment values of Co(II) complexes (**2** and **6**) are 2.46 and 4.84 BM, which submit to square planar and octahedral structures.[54,66,67] The magnetic moment value of Ni(II) complex (**3**) found to be 3.89 BM, which lies in the reported range (3.2–4.1 B.M.) for Ni(II) tetrahedral geometry.[68] Finally, the Th(IV) complex is diamagnetic as expected.[47]

The electronic spectrum of Fe(III) complex (**1**) showed a band at 548 nm (Table 3) assigned for the d–d transition
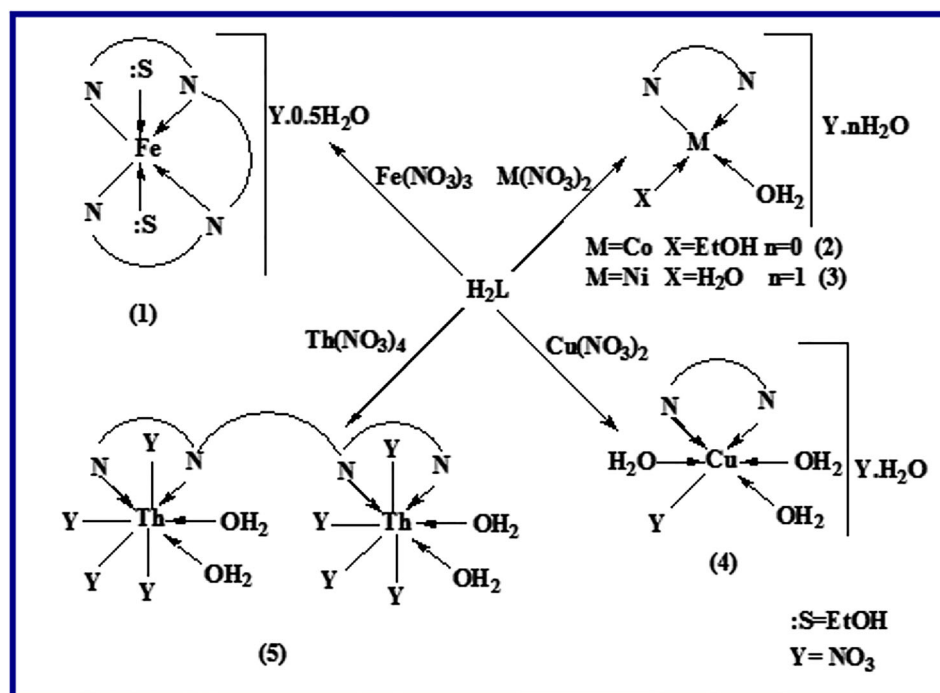
and/or strong charge transfer (CT) of octahedral structure of Fe(III) complex.[65,67,69–71] The electronic spectra of the Co(II) and Ni(II) complexes (**2 and 3**) showed bands at 593 and 499 nm, respectively, which refer to the $^2A_{1g}$–$^2B_{2g}$ and $^3T_1 \rightarrow {}^3T_1(P)$ transitions for Co(II) square planar[56] and Ni(II) tetrahedral[57] complex, respectively. However, Cu(II) complex exhibited band at 595, which refers to the $^2B_{1g} \rightarrow {}^2E_g$ transition for Cu(II) octahedral structure.[65,72,73] Whereas the electronic spectrum of the Co(II) complex (**6**) exhibited a band at 539 nm, it might arise from ^4T_1g (F) $\rightarrow {}^4A_2g(F)$ transition of Co(II) octahedral geometry.[67] The spectrum of Th(IV) complex showed a band at 333, which passes on to CT.[47]

3.2.3 | SEM

Figure 1 demonstrates the morphological structures of free ligand and its cobalt(II) complexes (**2 and 6**). The morphology of the ligand H$_2$BDTB that appeared as rod shape and changed by complexation with Co(II) ion in absence and presence of CTAB to irregular bulk sheets and fused aggregated clusters forms as shown for Co(II) complexes (**2 and 6**), respectively.

3.2.4 | ESR spectra

The ESR spectra at room temperature of Fe(III) and Cu(II) complexes (**1 and 4**) were chosen as representative
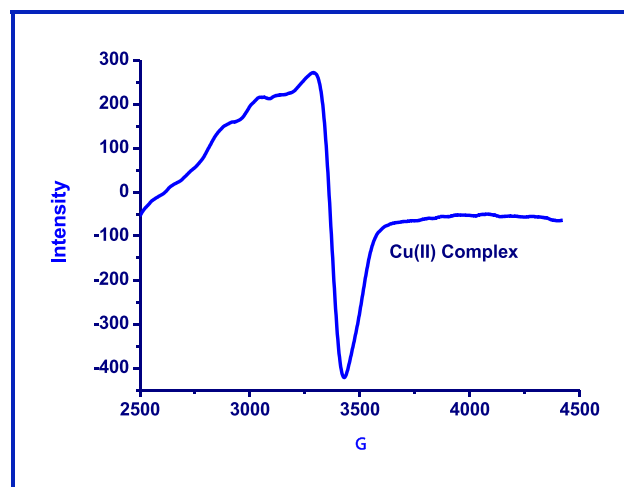

FIGURE 2 ESR spectrum of Cu(II) complex (**4**) at room temperature

examples. Figure 2 shows the ESR spectrum of Cu(II) complex (**4**) that is consistent with the octahedral geometry.[74,75] The ESR spectra of Fe(III) and Cu(II) complexes (**1 and 4**) have ($g_\perp$ = 2.009 and g_{II} = 2.028) and ($g_\perp$ = 2.1146 and g_{II} = 2.1629), with g_{iso} values of the complexes 2.01537 and 2.13069, respectively.[20,30,31] The calculated exchange interaction parameter (*G*) found to be 1.42 for Cu(II) complex (**4**), which is much lower than 4, referring to high copper

exchange interactions, reveals some ferromagnetic interaction as detected from the higher magnetic value (2.14 BM).

3.2.5 | ^{1}HNMR spectra

^{1}HNMR data are relative to TMS that recorded in DMSO-d_6 without and with D_2O, for the present Th(IV) complex (**5**) to characterize the bonding modes of the ligand H_2BDTB with Th(IV) ion. The data obtained at chemical shifts (δ/ppm) are as follows: 7.28–7.76 (24 H, phenyl groups, m) and 7.78 (2H, CH=N, s), 11.09 (2H, NH of hydrazino, s).[30,31] The disappearing NH signal on deuteration, referring that the ligand (H_2BDTB) acts as neutral in case of Th(IV) complex (**5**). The signal of coordinated water molecules, which appeared at 3.35 δ/ppm, might overlapped with the water of DMSO signals.[75] These results agree with the data obtained from IR spectral studies.

3.2.6 | Mass spectra

Scheme 3 and Figure 3 exemplify the mass fragmentation patterns of Co(II) complex (**2**); it showed molecular ion peak at 808.65 a.m.u., which agrees with the molecular weight proposed to be 808.72. As shown in Figure 3, the mass spectrum of the investigated compounds is relatively complex and exhibited a large number of peaks that extended to m/e 808.65 a.m.u. The most significant features in the spectrum of investigated complex are the most abundant molecular ion peak due to the loss of C_7H_5N group of ligand fragment (m/e = 102.99 a.m.u.; 40.80%), nitrate (m/e = 62.10 a.m.u.; 23.24%), and the base peak due to phC≡Cph (m/e = 178.17 a.m.u.; 100.00%), which is characteristic for the current starting hydrazone triazine. On the other hand, the residue CoO's m/e value equals 75.45, 47.08%. A less abundance peak was observed at different m/e positions depending on the other coordinating species. The extent of fragmentation
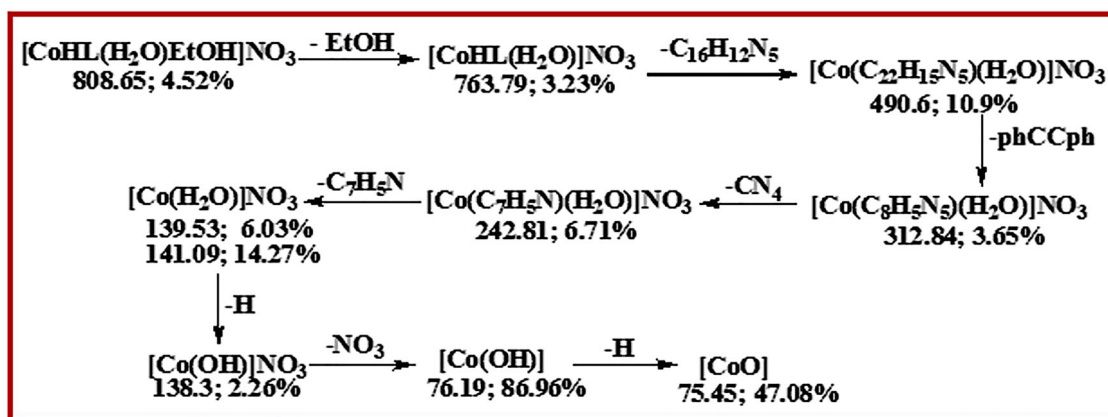
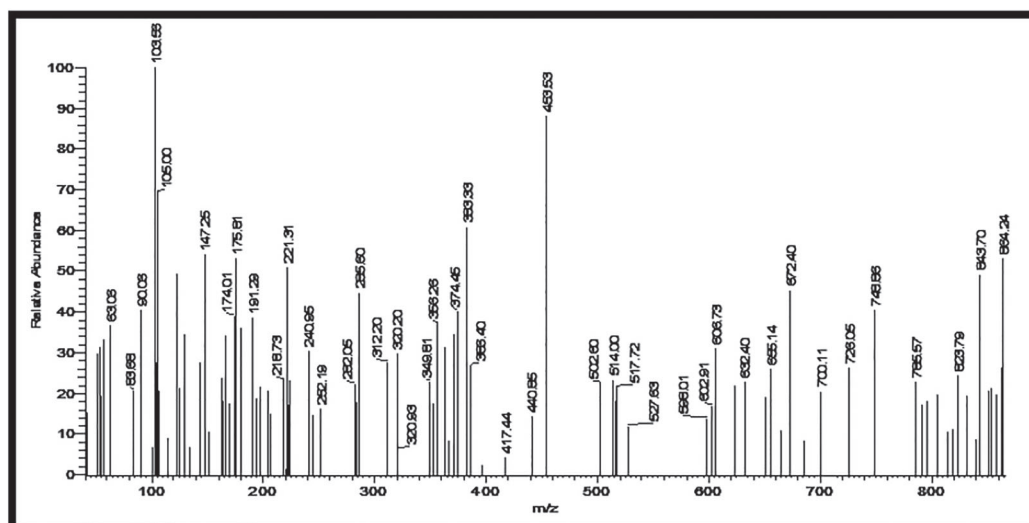**SCHEME 3** Mass fragmentation patterns of the Co(II) complex (**2**)

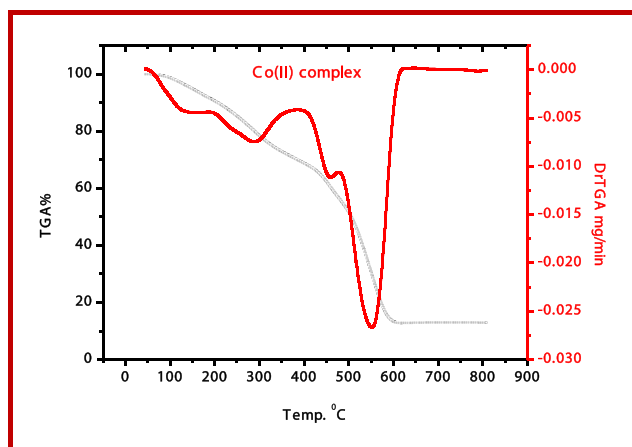**FIGURE 3** Mass spectrum of the Co(II) complex (**2**)

FIGURE 4 TGA diagram of the Co(II) complex (**2**)

of the molecular ion is inversely proportional to the relative stability of the complex, which depends on the type of metal ion.[76]

3.2.7 | TGA

TGA data extracted from the curves presented in Figure 4, Scheme 4, and Figure S1 of the current compounds are collected in Table 4. Some information and physical parameters are concluded, such as thermal stability hydrated or coordinated water molecules and thermal decomposition stages. The results collected in Table 4 reveal good agreements of the proposed formula weight with that expected from the analytical and spectral data.
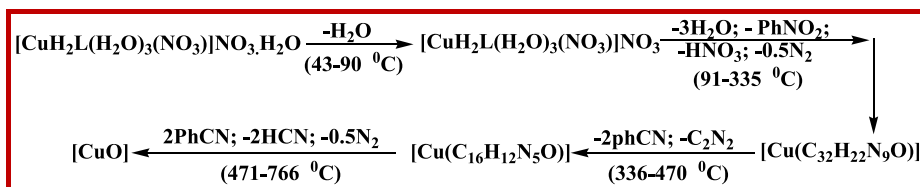
SCHEME 4 TGA fragmentation patterns of Cu(II) complex (**4**)

TABLE 4 Thermal analyses data (TGA) of H_2BDTB complexes

| No. | Complex | ΔT_{max} | Temperature range (°C) | %Loss in wt. | | Assignment |
				Found	Calc.	
1	[FeL (EtOH)$_2$]NO$_3$.½H$_2$O	79	50–112	0.989	1.07	½ H$_2$O (lattice)
		229	113–276	27.78	27.21	2 EtOH; phNO$_2$; ½ N$_2$
		342	277–398	26.47	26.14	2 phCN; ½ N$_2$
		442	399–491	37.50	36.95	2 phCN; 2 C$_2$N$_2$; ½ H$_2$
			Above 492	7.26	8.55	Residue [FeO]
2	[CoHL(H$_2$O)EtOH]NO$_3$	141	46–191	8.26	7.91	H$_2$O; EtOH (coordinate)
		287	192–390	22.10	22.01	phNO$_2$; HCN; N$_2$
		447	391–480	13.25	12.74	PhCN
		543	481–800	43.41	43.53	3 PhCN; ½ H$_2$; 1½ N$_2$
			Above 801	12.98	13.72	Residue [CoO + 3C]
3	[NiHL(H$_2$O)$_2$]NO$_3$.H$_2$O	89	47–130	1.98	2.25	H$_2$O (lattice)
		224	131–286	21.64	21.67	2 H$_2$O; PhNO$_2$; ½ N$_2$
		341	287–388	10.69	11.65	PhNH$_2$
		488	389–999	53.09	52.10	2PhCN; Ph (CN)$_2$; 2 HCN; N$_2$
			Above 1,000	12.60	12.36	Residue [NiO + 2C]
4	[CuH$_2$L(H$_2$O)$_3$(NO$_3$)]NO$_3$.H$_2$O	69	43–90	1.71	2.04	H$_2$O (lattice)
		246	91–335	28.55	28.61	3 H$_2$O; PhNO$_2$; HNO$_3$; ½N$_2$
		422	336–470	29.70	29.17	2 PhCN; C$_2$N$_2$
		537	471–766	30.35	30.98	2 PhCN; 2HCN; ½N$_2$
			Above 767	9.69	8.99	Residue [CuO]

TGA of [FeL (EtOH)$_2$]NO$_3$.½H$_2$O (Figure S1a) shows three main stages of decomposition in the range 113–491°C, besides the shoulder in the range 50–112°C at ΔT_{max} = 79°C, that corresponds to liberation of half mole of lattice water calc./found: 1.07/0.99%.[77,78] However, the first stage observed in the temperature range 113–276°C corresponding to the mass loss (calcd./found%; 27.21/27.78%) may be attributed to the decomposition of 2 mol of EtOH, 1 mol of nitrobenzene, and ½ mol of nitrogen gas at ΔT_{max} = 229°C. The second stage within the temperature range 277–398°C with mass loss (calcd./found%; 26.14/26.47%) indicates the removal of ½ mol of nitrogen gas and 2 mol of benzonitrile at ΔT_{max} = 342°C. However, the third stage observed within the range 399–491°C with mass loss (calcd./found%; 36.95/37.50%) matches with 2 mol of benzonitrile, 2 mol of C$_2$N$_2$, and ½ mol of hydrogen gas at ΔT_{max} = 442°C, leaving FeO as residue.

However, [NiHL(H$_2$O)$_2$]NO$_3$.H$_2$O and [CuH$_2$L (H$_2$O)$_3$(NO$_3$)]NO$_3$.H$_2$O complex (**3** and **4**) thermograms showed four stages of decomposition pattern as shown in Scheme 4 and Figure S1b,c. The first stage within the temperature range 47–130 and 43–90°C at ΔT_{max} = 89 and 69°C, corresponding to the mass loss (calcd./found: 2.25/1.98% and 2.04/1.71%), respectively, indicates the removal of 1 mol of lattice water. However, the second stage obtained at the temperature ranges 131–286 and 91–335°C at ΔT_{max} = 224 and 246°C matches with the mass loss of 21.67/21.64% and 28.61/28.55% arising from the decomposition of 2 mol of coordinated H$_2$O, 1 mol of PhNO$_2$, and ½ mol of N$_2$ gas and 3 mol of coordinated water, 1 mol of PhNO$_2$, 1 mol of HNO$_3$, and ½ mol of N$_2$ gas, respectively. The third stage observed in the temperature ranges 287–388 and 336–470°C at ΔT_{max} = 341 and 422°C, corresponding to mass loss of 10.69% and 29.70%, attributed to the decomposition of aniline and (2 PhCN and C$_2$N$_2$), respectively. But the fourth stage observed in the temperature range 389–999 and 471–766°C at ΔT_{max} = 488 and 537°C is analogous to the decompositions of (2PhCN; Ph [CN]$_2$; 2 HCN and N$_2$) and (2 PhCN; 2 HCN and 0.5 N$_2$), comparable with 52.10/53.09% and 30.98/30.35%, respectively. In the end, the residue is found to be 12.60/12.36 and 8.99/9.69% corresponding to NiO with carbon residue and CuO, respectively.

Finally, the thermogram of the [CoHL(H$_2$O)EtOH]NO$_3$ complex (**2**) confirmed that both coordinated water and ethanol eliminated in the range 46–191°C at ΔT_{max} = 141°C (Figure 4), matched to 7.91/8.26%. However, the decomposition observed in the range 192–390°C at ΔT_{max} = 287°C is analogous to the fragments of 1 mol of nitrobenzene, 1 mol of hydrogen cyanide, and 1 mol of nitrogen gas. The third stage detected at 391–480°C at ΔT_{max} = 447 °C, corresponding to a mass loss of 12.74/13.25%, correlated to 1 mol of benzonitrile. On the other hand, the decomposition observed in the range 481–800°C at ΔT_{max} = 543°C is analogous to the fragments of 3 mol of benzonitrile, ½ mol of hydrogen gas, and 1½ mol of nitrogen gas, leaving CoO in addition to carbon as residue.

The calculated kinetic parameters are summarized in Table 5, which remarks the following points:

a. The rate of decomposition of the second stage is higher than that of the first stage, which is opposite to their activation energies.

TABLE 5 Temperature of decomposition and activation parameters (E*, ΔH^*, ΔS^*, and ΔG^*) determined from TGA results for the decomposition of H$_2$BDTB complexes

No.	Complex	Stage	E* (KJ/mol)	A (S^{-1})	ΔH^* (KJ/mol)	ΔS^* (KJ/mol.k)	ΔG^* (KJ/mol)
1	[FeL (EtOH)$_2$]NO$_3$.½H$_2$O	1st	69.73	69.07	7x10^9	117.8	59.77
		2nd	31.69	29.79	142.63	−38.60	38.62
		3rd	63.52	60.68	74,654	10.12	57.22
2	[CoHL(H$_2$O)EtOH]NO$_3$	1st	43.98	42.81	55,322	14.99	40.70
		2nd	13.95	11.57	0.8596	−82.90	35.36
		3rd	13.53	9.816	0.3285	−94.60	52.10
3	[NiHL(H$_2$O)$_2$]NO$_3$.H$_2$O	1st	81.29	80.55	2x10^{11}	144.9	67.65
		2nd	34.29	32.43	357.32	−30.80	39.32
		3rd	7.158	4.325	0.0997	−102	39.20
4	[CuH$_2$L(H$_2$O)$_3$(NO$_3$)]NO$_3$.H$_2$O	1st	77.76	77.19	4x10^{11}	151.6	66.73
		2nd	15.86	13.81	----	-----	----
		3rd	26.15	22.64	6.4969	−69.3	51.90

Note: E* and A are the activation energy and the Arrhenius pre-exponential factor, respectively.

b. The values of ΔH^* and ΔG^* are positive, revealing an endothermic and nonspontaneous decomposition processes.

c. The products are less ordered than that of reactants for most stages, where they have positive values of ΔS^* in these stages.[68]

3.3 | Fluorescence studies

3.3.1 | Effect of solvents on the steady-state absorption and emission spectra

The measurement of photophysical properties of ligand (H_2BDTB) and its Fe(III) and Th(IV) complexes (**1** and **5**) were chosen—as representative examples—in various solvents polarities to investigate their applicability as fluorescent models and investigate their solvatochromic behavior and estimate the dipole moments of ground and excited states.

The change in the solvent polarity can modify the energy gap between the ground and singlet excited states, therefore leading to changes in the position, intensity, and shape of the emission bands. Hence, the solvent polarity directly measures the specific solute–solvent interaction between the molecules. The values of solvent parameters dielectric constant (ε) and refractive index (n) along with their polarity functions are calculated as described in our previous work and used in the present study.[79,80]

All the spectroscopic data (absorption, emission maxima, wave number, and spectral shift) of the H_2BDTB and its Fe(III) and Th(IV) complexes (**1** and **5**) in various solvents are collected in Table 6. The data in Table 6 expose excitation maxima at 290, 285, and 280 nm,

displaying fluorescence maxima between 339 and 491, 350 and 375, and 333 and 423 nm, with shift 152, 25, and 90 nm, respectively. The smaller shift of the absorption band with the change of solvent polarity refers to a lesser polarity of their ground state rather than the excited state. Consequently, the predictable value of ground state dipole moment (μ_g) would be smaller than excited state (μ_e). As soon as dipole moment of solute increases during the excitation, a positive solvatochromism on the average results.[79]

The magnitudes of Stokes shifts ($\Delta\nu = \nu_a - \nu_f$, where "$\nu_a$ and ν_f refer to the wave numbers of absorbance and fluorescence bands") with the change of solvent polarities are detected (Table 6) in the ranges 4984.23–14116.2, 6516.29–8421.05, and 5684.26–12073.6 cm^{-1} for free ligand (H_2BDTB) and Fe(III) and Th(IV) complexes (**1** and **5**), respectively. This large Stokes shift indicates the CT transition with the geometry change of the excited state than that of the ground state. The general inspection of the data in Table 6 reveals increasing Stokes shift with the increase of solvent polarity. Consequently, the dipole moment increases upon excitation; so, excited state will be energetically stabilized relative to the ground state among increasing solvent polarity with a noticeable redshift of fluorescence.

3.3.2 | Solvatochromism and estimation of ground and excited state dipole moments

Solvatochromism describes the change in position of a spectroscopic band, absorption or emission, caused by a change in solvent polarity; the shifts are due to the solute–solvent interactions. In specific type of interaction, shifts are due to hydrogen bonding, n-donor, and π-donor

TABLE 6 Excitation and emission (λ_{em}/nm) spectral data of H_2BDTB and its Fe(III) and Th(IV) metal ions in different solvents, at room temperature

Solvent	(H_2BDTB) (290)[a]		Fe(III) complex (285)[a]		Th(IV) complex (280)[a]	
	λ_{em}/nm	Stoke/cm^{-1}	λ_{em}/nm	Stoke/cm^{-1}	λ_{em}/nm	Stoke/cm^{-1}
1,4-Diox	347	5664.31	350	6516.29	340	6302.52
Toluene	355	6313.74	370	8060.69	370	8687.26
Ether	339	4984.23	354	6839.13	333	5684.26
EtOH	354	6234.17	356	6997.83	413	11501.2
MeOH	355	6313.74	358	7154.76	423	12073.6
DMF	349	5829.46	358	7154.76	342	6474.52
MeCN	491	14116.2	375	8421.05	-	-
Water	357	6471.55	360	7309.94	413	11501.2

[a]λ excitation/nm.

of the solvents. In order to estimate the ground and excited state dipole moments, solvatochromic shift method correlates spectral shift (Stokes shift "$\Delta \nu$" or average of absorption "ν_a" and fluorescence "ν_f" wave numbers) with solvent polarity as given by Lippert–Mataga, Bakhshiev, Kawski–Chamma–Viallet, and Reichardt correlations as described earlier.[79–85] Equations 1–4 were applied to estimate the dipole moments of ground (μ_g) and excited (μ_e) states of the current compounds.

$$Stokes\ shift = m_1 F_{L-M}(\varepsilon, n) + C_1 \quad (1)$$

$$Stokes\ shift = m_2 F_B(\varepsilon, n) + C_2 \quad (2)$$

$$½\left(\nu_a + \nu_f\right) = m_3 F_{K-C-V}(\varepsilon, n) + C_3 \quad (3)$$

$$Stokes\ shift = m_4 E_T^N + C_4 \quad (4)$$

where Stokes shift $(\Delta \nu) = \nu_a - \nu_f$; ν_a and ν_f are the absorption and fluorescence maxima, and n and ε are

the refractive index and the dielectric constant of the solvents, respectively, E_T^N is the normalized solvent-polarity parameter proposed by Reichardt.[79] The expressions for the slopes (m_1, m_2, m_3, and m_4) and solvent polarity F_{L-M}, F_B, and F_{K-C-V} as well as E_T^N functions and intercepts (C_1–C_4) are given in Table 7, such as described in our previous works.[79,80a]

It can be seen that from the data in Table 7, the correlation coefficients (r) are found to be in the range (0.91–0.98); they are obtained by using maximum number of points fitted to get the good linearity for these correlations. Deviation of some points from linearity may be recognized as due to short-range specific solute–solvent interactions.

The slopes of correlations given in Table 7 are used to calculate the ground (μ_g) and excited (μ_e) states, in addition to their differences in dipole moments ($\Delta\mu$), such as described previously.[79] The dipole moment ratio (μ_e/μ_g), Onsager cavity radius, and angle between dipole moment vectors of the present complexes are also calculated and collected in Table 8.

The ground state dipole moment values (2.705, 3.396, and 8.154 D) are lower than the singlet excited state

TABLE 7 Linear regression analysis data obtained from various plots of solvatochromic methods for the H_2BDTB and its Fe(III) and Th(IV) complexes

No.		Slope (m)	Intercept (C)	R	N	Solvents
H_2BDTB	m_1	2407.1	5606.5	0.98	4	Diox., EtOH, MeOH, water
	m_2	840.59	5619.8	0.98	4	Diox., EtOH, MeOH, water
	m_3	−15,251	37,730	0.97	4	Diox., toluene, ether, acetonitrile
	m_4	1038.1	5483.1	0.98	4	Diox., toluene, ether, acetonitrile
	$M_5\varphi$	−12,213	71,890	0.92	5	Diox., EtOH, MeOH, DMF, water
1	m_1	2342.1	6457.2	0.96	5	Diox., ether, EtOH, MeOH, DMF, water
	m_2	778.02	6498.2	0.96	5	Diox., ether, EtOH, MeOH, DMF, water
	m_3	−656.38	32,017	0.92	4	Diox., ether, EtOH, MeOH, DMF
	m_4	794.05	6520.5	0.94	5	Diox., ether, EtOH, MeOH, water
	$M_5\varphi$	−811.89	64,109	0.94	5	Diox., ether, EtOH, MeOH, DMF, water
5	m_1	14,378	7278.1	0.93	5	Diox., Toluene, EtOH, MeOH, water
	m_2	5032.8	7344	0.93	5	Diox., Toluene, EtOH, MeOH, water
	m_3	−7669.3	35,323	0.92	6	Diox., Toluene, ether, EtOH, MeOH, water
	m_4	11,147	3515.9	0.95	5	Diox., ether, EtOH, MeOH, DMF
	$M_5\varphi$	−6378.1	68,162	0.95	5	Diox., toluene, EtOH, MeOH, water

TABLE 8 Onsager cavity radius (a/Å) and ground state and excited state dipole moments (μ_g and μ_e/D), calculated by theoretical and experimental methods for the ligand H_2BDTB, Fe(III), and Th(IV) complexes

No.	a/Å	μ_g^a	μ_g^b	μ_e^b	μ_e^c	μ_e^d	μ_e^b/μ_g^b	$\Delta\mu^d$
H_2L	6.913	2.963/5.131	2.705	6.016	7.415	12.677	2.224	5.513
1	7.616	10.26	3.396	6.768	5.404	5.3975	1.993	3.247
5	7.594	-	8.154	16.936	18.735	12.678	2.077	12.113

dipole moments (6.016, 6.768, and 16.936 D) for free H$_2$BDTB and its Fe(III) and Th(IV) complexes (**1** and **5**), respectively. The solvent–solute interactions of the investigated compounds are lesser polarity in ground states than in their excited states. This might attributed to the redistribution of charge densities between both electronic states that arises from the $\pi \rightarrow \pi^*$ transitions of the present compounds.

As observed from the data collected in Table 8, the theoretical values of ground state dipole moment (μg*) that obtained from *Hyperchem* 7.52 software at *PM3* semiempirical level for Fe(III) complex (**1**) for free H$_2$BDTB and Fe(III) complex (**1**) are found to be 2.963 and 7.73 D and 10.26 D, respectively, calculated by *PM3* and DFT at basis set 6-31G, compared with that estimated from solvatochromic shift, 2.705 and 3.396 D. The discrepancy could be on one side due to the oversimplification used in solvatochromic methods and strong specific effects of the solvents. On the other side, theoretical calculations give dipole moment values only for molecule in a gas phase.[80]

Quantitative analysis of the specific and nonspecific interactions using linear solvation-free energy relationships (LSFER) for the Stokes shift ($\Delta\nu$) versus various solvent parameters are collected in Table S1, which points to the following points:

a. Bathochromic shift of the emission band enhanced by increasing Lewis acidity (AN) of solvent, evidenced by the positive slopes of AN of solvents versus $\Delta\nu$ data of H$_2$BDTB and Th(IV) complex. This means that H$_2$BDTB and Th(IV) complex (**5**) work as Lewis bases in the present study. The slope in the case of Th(IV) complex (**5**) (143.24) is much higher than that of the ligand (25.353), which means that the Lewis basicity of Th(IV) complex (**5**) is about six times of free ligand.

b. The positive slopes of hydrogen bond donor (HBD) (α) versus $\Delta\nu$ relationships reveals that the present probes (H$_2$BDTB and Fe(III) and Th(IV) complexes [**1** and **5**]) act as hydrogen bond acceptor (HBA). This finding is further established by the negative slope of HBA (β) versus $\Delta\nu$ of Fe(III) complex (**1**) as given in Table S1. The extent of the HBD effect can be deduced from their slope coefficient ratios, 1.2:1:9.6, for H$_2$BDTB, Fe(III), and Th(IV) complexes (**1** and **5**), respectively.

c. The positive slopes of E$_T$ with $\Delta\nu$ relationships imitate the extent of specific solute–solvent interaction through solvent polarity with the ratio 11:2:1, as deduced from their slope coefficient ratios for Th(IV) complex: H$_2$BDTB:Fe(III) complex, respectively.

d. Comparison of π, β, and α contributions for Fe(III) complex (**1**) emission spectra designates that the π^*

(nonspecific) has similar to the effect of α (specific), because they have positive signs effect with nearly coefficient values. However, β (specific) has opposite effect (negative sign) with a three times extent, as indicated from their slope coefficient ratios 1:1:3 (π^*:α:β). Thus, the specific solute–solvent interaction plays the major role in the emission spectra.

A common inspection points to the increase in Stokes shift with the increase of solvent polarity, referring to increase in the dipole moment upon excitation. In such cases, the relaxed excited state S1 will be energetically stabilized compared with their ground state S0, and hence, a significant redshift of the fluorescence will be observed as noticed from the present data.

3.3.3 | Biological activity

Antimicrobial activity

Table 9 showed antimicrobial activity of H$_2$BDTB and its complexes. They have activity against Gram-positive bacteria and *C. albicans*, but they have not activity toward *S. typhimurium* (ATCC 14028) and *A. fumigatus* as demonstrated in Figure 5. The H$_2$BDTB has low activity toward *B. subtilis* and moderate activity against *E. coli and C. albicans*. Co(II) and Ni(II) complexes (**2** and **3**) have similar antimicrobial activity; they exhibited low activity against (*S. aureus* and *B. subtilis*) and moderate activity against *C. albicans*, similar to the H$_2$BDTB. However, the activity of the Cu(II) complex (**4**) is higher than the other complexes, which showed intermediate activity to *B. subtilis* and high activity against *C. albicans*.[31] On the other hand, Th(IV) complex has intermediate activity toward *C. albicans*, but Fe(III) complex (**1**) shows no antimicrobial activity, for these microbial in the present range of concentrations, 1.0–0.5 μg.

Antitumor activity

The antitumor activity of the ligand (H$_2$BDTB) and Co(II) and Ni(II) complexes (**2**, **3**, and **6**), taken as representative examples, has been determined (Figure 6). The antitumor activity of H$_2$BDTB is less than its Co(II) and Ni(II) complexes (**2** and **3**), where IC$_{50}$ = 230, 27.7, and 74.3 μg/ml, respectively. This finding might attribute to the increase of the ligand skeleton conjugation by complexation with Co(II) and Ni(II) ions.[47,86] However, the Co(II) complex (**6**) showed IC$_{50}$ = 5.73 μg/ml, which is less than the value of the antitumor drug (cisplatin, 15.9 μM), promising that complex (**6**) can be nominated as one of the most powerful antitumor drugs.

TABLE 9 Antimicrobial activity of the H₂BDTB and its complexes

Mean^a of zone diameter, nearest whole mm

Organisms	Gram-positive bacteria				Gram-negative bacteria				Yeasts and fungi^b			
	Staphylococcus aureus (ATCC 25923)		Bacillus subtilis (ATCC 6635)		Salmonella typhimurium (ATCC 14028)		Escherichia coli (ATCC 25922)		Candida albicans (ATCC 10231)		Aspergillus fumigatus	
Sample Conc/no.	1 mg/ml	0.5 mg/ml	1 mg/ml	0.5 mg/ml	1 mg/ml	0.5 mg/ml	1 mg/ml	0.5 mg/ml	1 mg/ml	0.5 mg/ml	1 mg/ml	0.5 mg/ml
H₂L	-	-	10 L	7 L	-	-	13 I	9 I	19 I	15 I	-	-
1	-	-	-	-	-	-	-	-	-	-	-	-
2	10 L	8 L	9 L	7 L	-	-	-	-	19 I	15 I	-	-
3	11 L	8 L	9 L	7 L	-	-	-	-	20 I	15 I	-	-
4	-	-	19 I	15 I	-	-	-	-	36 H	29 H	-	-
5	-	-	-	-	-	-	-	-	15 I	10 I	-	-
Control #	35	26	35	25	36	28	38	27	35	28	37	26

Abbreviations: −, no effect; #, chloramphenicol in the case of Gram-positive bacteria, cephalothin in the case of Gram-negative bacteria, and cycloheximide in the case of fungi; H, high activity = mean of zone diameter > 2/3 of mean zone diameter of control; I, intermediate activity = mean of zone diameter ≤ 2/3 of mean zone diameter of control; L, low activity = mean of zone diameter ≤ 1/3 of mean zone diameter of control.

^aCalculated from three values.

^bIdentified on the basis of routine cultural, morphological, and microscopical characteristics.
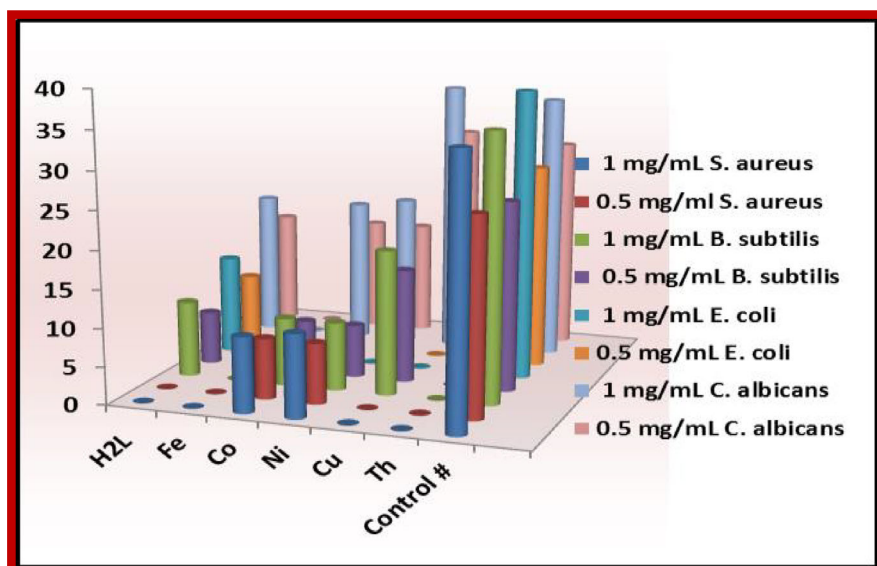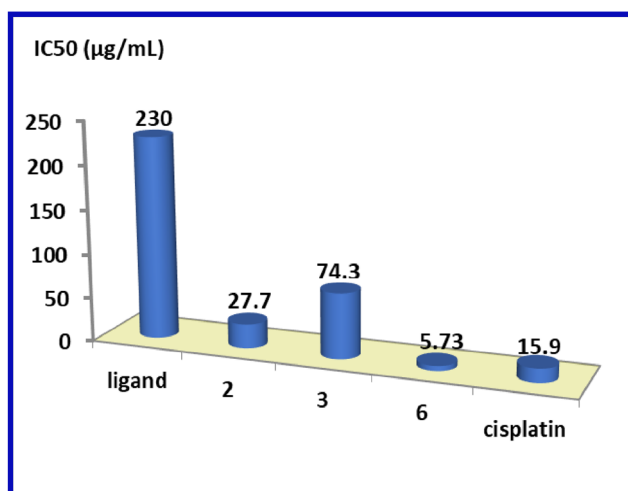
FIGURE 6 Graph showing comparative result of inhibition concentration 50% (IC$_{50}$) from antitumor activity of the H₂BDTB, Ni(II), and Co(II) complexes (**3**, **2**, and **6**) against HepG-2

3.4 | Molecular docking

Because c-Met residues are the membrane receptor for hepatocyte growth factor (HGF), it is documented previously to cause dysregulation when mutated in several cancers.[87] This provoked us to carry out molecular docking studies. to investigate the underlying mechanism of possible molecular interaction of these compounds with c-Met tyrosine kinase and the receptor of hepatocyte growth factor/scatter factor (HGF/SF) using MOE against all the predicted active sites via extracellular alpha chain and a transmembrane beta chain. In the current work, c-Met tyrosine kinase (PDB ID: 3ce3) interacts with

H₂BDTB compounds as inhibitors. Validation of the molecular docking protocol was first performed by re-docking of the co-crystallized ligand, H₂BDTB. The re-docking validation step reproduced the experimental binding pattern of the co-crystallized ligand efficiently, indicating the suitability of the used docking setup for the planned docking study. Interaction results were evaluated with the S-score inhibitors with the lowest S-score tending to establish a strong interaction with c-Met tyrosine kinase on specific active sites (Table 10). The RMSD of 3ce3, H₂L, and its complexes (**1–4** and **6**) are equal 0.79, 1.05, 1.42, 1.59, 1.21, 1.18, and 1.38, respectively; this represents good reproduction of the correct pose. The results showed that all compounds were in the pocket of the target protein c-Met tyrosine kinase. The binding energy score is -7.9562, -7.3829, -8.6629, -8.6403, -9.6443, and -6.7789 kcal/mol for H2BDTB and its complexes (**1–4** and **6**), respectively. After docking, we recognized a compound showing minimum S-score among all the inhibitors. Cu(II) complex (**4**) showed a minimum S-score of -9.6443. Therefore, it establishes the strongest interaction with c-Met tyrosine kinase among all the inhibitors discussed in this study. However, Co(II) complex (**6**) was predicted to exhibit a least binding affinity for c-Met tyrosine kinase, with an S-score of -6.7789 kcal/mol.

The free ligand (H₂BDTB) formed two bonds with the amino acid residues: One of them is H-donor bond between the NH of the amidic on the triazine moiety $N_{triazine}$ of H₂BDTB and HIS 1202 (distance $= 3.44$ A° -0.8 Kcal/mol). The second bond is pi–H bond between triazine of H₂BDTB ligand and PHE 1200 (distance $= 4.14$ A°; E $= -0.6$ kcal/mol). It is notable

TABLE 10 The molecular docking data for the H$_2$BDTB and its complexes (**1–4** and **6**) by using MOE 2014.0901 software (PDB. I.D.3ce3)

No. of compound	Compound part	Amino acid	Interaction	Distance	E (kcal/mol)	The binding energy score (S)	# of bonds
H$_2$L	N of triazine ring	HIS 1202	H-donor	3.44	−0.8	−7.9562	2
	6-ring	PHE 1200	pi–H	4.14	−0.6		
1	O of water molecule	LYS 1244	H-donor	2.72	−5.3	−7.3829	1
2	O of water molecule	ASP 1222	H-donor	2.85	−7.5	−8.6629	2
	6-ring	HIS 1088	H–pi	4.07	−0.9		
3	O of water molecule	GLY 1224	H-donor	2.83	−2.2	−8.6403	1
4	O of water molecule	ILE 1084	H-donor	3.26	−0.9	−9.6443	4
	N of triazine ring	LYS 1110	H-acceptor	3.39	−0.8		
	6-ring	LYS 1110	pi–cation	3.47	−1.9		
	6-ring	GLY 1224	pi–H	4.58	−1.7		
6	O76 of water molecule	GLU 1127	H-donor	3.12	−4.9	−6.7789	3
	O79 of water molecule	ASP 1222	H-donor	2.75	−4.2		
	6-ring	LYS 1244	pi–H	4.28	−1.3		

that free ligand revealed a moderate binding energy score (S = −7.9562 kcal/mol) (Figure 7a).

However, Fe(III) complex (**1**) formed one H-donor bond between O of water molecule and LYS 1244 (2.72 A° −5.3 kcal/mol). On the other hand, Co(II) complex (**2**) (Figure 7b) formed two bonds with the amino acid residues: The first is H-donor bond between O of water molecule and ASP 1222 (2.85 A° −7.5 kcal/mol), and the second bond is H-pi bond between 6-ring of the ligand moiety and HIS 1088 (4.07 A° −0.9 kcal/mol), but Ni(II) complex (**3**) formed one H-donor bond between O of water molecule and GLY 1224 (2.83 A° −2.2 kcal/mol).

However, Cu(II) complexes (**4**) formed four bonds with the amino acid residues in the active site of protein. The first hydrogen bond is between O of water molecule and ILE 1084 (3.26 A° −0.9 kcal/mol.). The second bond is H-acceptor between N$_{triazine}$ of H$_2$BDTB ligand and LYS 1110 (3.39 A° −0.8 kcal/mol.). The third bond is pi-cation between 6-ring of H$_2$BDTB ligand and LYS 1110 (3.47 A° −1.9 kcal/mol.). The last bond is pi–H between 6-ring of H$_2$BDTB ligand and GLY 1224 (4.58 A° −1.7 kcal/mol.). On the other hand, Co(II) complex (**6**) (Figure 7c) formed three bonds with the amino acid residues and two H-donor bond between O$_{76}$ of water molecule with GLY 1227 (3.12 A° −4.9 kcal/mol.) and O$_{79}$ of another water

molecule with ASP 1222 (2.75 A° −4.2 kcal/mol.). The third bond is pi–H bond between 6-ring of the H$_2$BDTB and LYS 1244 (4.28 A° −1.3 kcal/mol.).

The antitumor activity date of H$_2$BDTB and Co(II) and Ni(II) complexes (**2**, **3**, and **6**) (IC50 = 230, 27.7, 74.3, and 5.73 μg/ml, respectively) agreed with QSAR and docking results collected in Table S4, where Co(II) complex (**6**) has the smallest surface area (884.66) and molar volume (1690.67), which might facilitate it to penetrate the antitumor cells. Furthermore, the complex (**6**) interactions with the key active site of amino acid residues by three bonds, which have short distances from these sites, consequence a strong bond formation with total energies (−10.40 kcal/mol), in comparison with the corresponding data of other compounds under investigation. This might enhance the strong binding of Co(II) complex (**6**) with the antitumor cells, as it has IC50 = 5.73 μg/ml, which is stronger than antitumor drug (cisplatin, IC50 = 15.9 μM).

The docking data agreed also with the antimicrobial activity data of H$_2$BDTB and its complexes (**1–4**), where Cu(II) complex (**4**) has highest antimicrobial activity and formed two H bonds and two pi bonds and S-score (−9.6443). Moreover, Cu(II) complex (**4**) has small molar volume (1802.69) and high hydration energy (−34.56) as
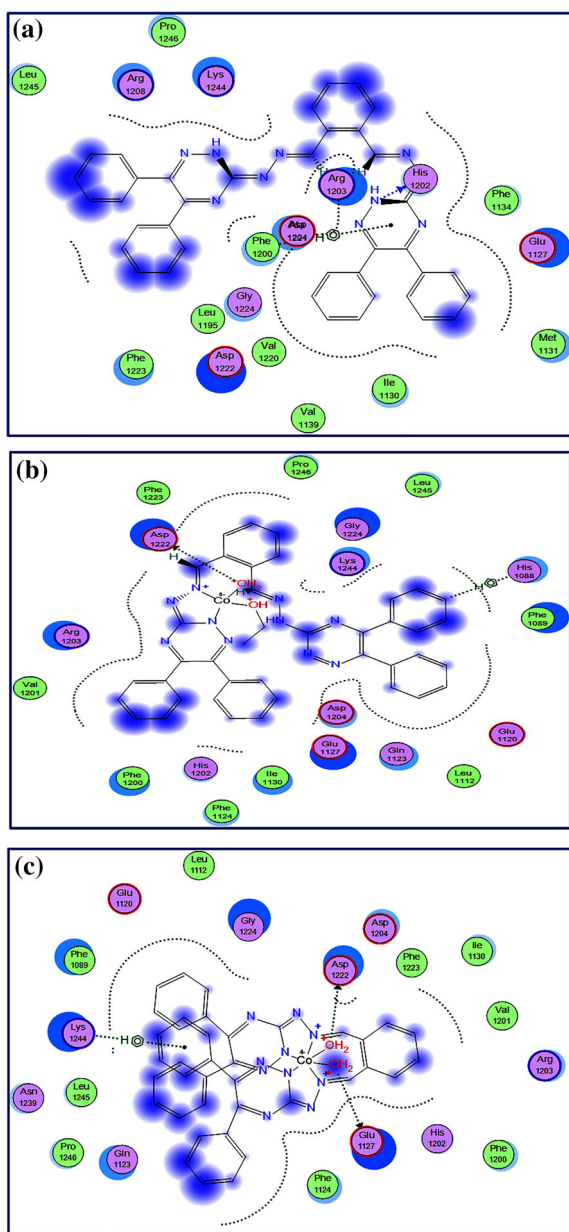
FIGURE 7 (a) 2D interactions of the H_2BDTB tautomer (II) with the active site amino acid residues of protein (PDB. I.D.3ce3). (b) 2D interactions of Co(II) complex (**2**) with the active site amino acid residues of protein (PDB. I.D.3ce3). (c) 2D interactions of Co(II) complex (**6**) with the active site amino acid residues of protein (PDB. I.D.3ce3)

shown in Table S4, subsequently smoothing the progress of cell penetration of the cell wall. However, the other compounds formed one H bond only/and one pi bond for the H_2BDTB ligand and its complexes (**1–3**). The current results show that all members of this series of compounds were able to recognize the active site of the c-Met kinase and perform different types of bonding interactions with the key active site of amino acid residues.

3.5 | Molecular orbital calculations

The optimized structures of ligand (H_2BDTB) and its complexes, except Th(IV) complex (**5**), were performed by *Hyperchem 7.52* program using semi-empirical (*PM3* level), in addition to *Gaussian 09* using DFT at basis set 6-31G. The structural parameters were calculated and summarized in Table 11. The molecular stability and reactivity depend on global hardness (η) (2.69–5.038 eV), global softness (S) (0.129–0.652 eV^{-1}), and softness (σ) (0.127–0.372 eV^{-1}) values, where hard complexes are less reactive than soft compounds, where electrons transfer to an acceptor.[88] The electronegativity (χ) is 1.535–5.543 eV, and the global electrophilicity index (ω) 1.702–5.711 eV. The tautomeric form (I) has a low positive heat of formation than that of the tautomer (II), which refers that the tautomer (I) is more stable than the other the tautomer (II).[30,31]

The strength of $C=N_{azomethine}$ and (C=N and N–N)$_{triazine}$ bonds is decreased by coordination of ligand to metal ion (Table S2).[11,30,31] The relation between E_{LUMO} and $C=N_{azomethine}$ of the H_2BDTB and its metal complexes and their reactivity toward *B. subtilis* and *C. albicans* points to the Cu(II) complex (**4**) has highest −ve E_{LUMO}, +ve $C=N_{azomethine}$ values and reactivity toward *B. subtilis* and *C. albicans*.

The good correlations between theoretical and experimental data were reported in Table S3. We can conclude the following remarks:

a. The increasing of interaction between metal and the nitrogen atom of the ligand (H_2BDTB) leads to the increase of (C–N)T bond length as well as the decrease of M–N bond length and λ_{max}.[30,31]
b. The relation between frequencies and lengths of $C=N_{azomethine}$ bonds refers to by complexation, increase in bond lengths, and decrease in frequencies of $C=N_{azomethine}$ bonds.[30,31]
c. The negative slope of the relation between the frequencies of (C=N)T bonds with E_{LUMO} refers to increasing of E_{LUMO}, accompanied by decreasing (C=N)T frequencies.[31,89]

Table S4 showed that QSAR properties of complexes increased than that of H_2BDTB such as surface area, volume, log p (tautomer I), refractivity (tautomer II), and polarizability. Hydration energy of H_2BDTB changes from −20.66 to −26.81 to −11.30 to −35.87 kcal/mol.[90]

DFT calculations (631G) were performed on the ligand and its cobalt(II) complex (**2**) using Gaussian 09 program package.[45] Table 11 showed structural parameters of the H_2BDTB and its metal complexes from

TABLE 11 Structural parameters of the H_2BDTB and its metal complexes obtained at semiempirical (*PM3*) and DFT calculations (6-31G) levels using *Hyperchem 7.52 and* Gaussian 09 programs

No.	Heat of formation, kcal/mol	Dipole moment [μ/D]	HOMO energy, [eV]	LUMO energy, [eV]	ΔE_{gap} [eV]	η [eV]	σ [eV^{-1}]	S [eV^{-1}]	χ [eV]	ω [eV]
	Semiempirical (*PM3*) level using *Hyperchem 7.52* program									
H_2L^a	336.7296	2.963	−8.874	−1.104	7.770	3.885	0.257	0.129	4.989	3.203
H_2L^b	366.513	5.131	−8.981	−1.094	7.887	5.038	0.127	0.254	3.944	3.217
1	−112.486	10.26	−7.1303	−1.0000	6.130	4.065	0.163	0.326	3.065	2.696
2	59.577	5.786	−8.4253	−1.0648	7.361	4.745	0.136	0.272	3.680	3.059
3	73.133	8.889	−3.820	−0.751	3.069	2.286	0.326	0.652	1.535	1.702
4	98.367	11.630	−8.233	−2.853	5.380	2.690	0.372	0.186	5.543	5.711
6	−84.165	5.123	−7.550	−1.117	6.433	3.217	0.311	0.155	4.334	2.919
	DFT calculations (631G) using Gaussian 09 program package									
H_2L^a	−1259.348	7.729	−5.395	−2.236	3.159	1.58	0.633	0.317	3.815	4.607
2	−2286.290	6.5706	−4.144	−1.933	2.211	1.105	0.905	0.452	3.039	4.176

[a]L tautomer (**I**).
[b]L tautomer (**II**).

two similar programs. The bond length of C=N for triazine and azomethine increases by complexation.

4 | CONCLUSION

The new bistriazine ligand (H_2L) H_2BDTB has two tautomers, and its metal complexes are synthesized and characterized by several techniques. Octahedral environments have been proposed for Fe(III), Cu(II), and Co(II) metal ions (**1**, **4**, and **6**), but tetrahedral for Ni(II) complex (**3**) and square planar for the Co(II) complex (**2**). All the complexes are electrolytes (1:1), except for the Th(IV) complex (**5**), which is non-electrolyte. The ligand acts as a monobasic bidentate for all mononuclear complexes, except for the Cu(II) complex (**4**), in which the ligand acts as neutral bidentate. On the other hand, the ligand acts as neutral tetradentate for binuclear Th(IV) complex (**5**) and as dibasic tetradentate for the Fe(III) and Co(II) complexes (**1** and **6**). Good correlations were detected between experimental data and theoretical data of the present compounds extracted from DFT at 631-G and *PM3* levels by means of Gaussian 09 and *Hyperchem* programs. The two triazine moieties in the H_2BDTB and its complexes are responsible for biological activities. The Co(II) complex (**6**) showed IC_{50} = 5.73 μg/ml, which is less than the value of the antitumor drug (cisplatin) (15.9 μM), which designated it as one of the most powerful antitumor drugs. The molecular docking data obtained using molecular operating environment MOE 2014.0901 software (PDB. I.D.3ce3) allowed us to observe the interactions with protein and compounds.

CONFLICT OF INTEREST

The authors of the article do not have any conflict of interest.

AUTHOR CONTRIBUTIONS

Fatma Samy: Conceptualization; formal analysis; investigation; methodology; software; visualization. **Ali Taha:** Conceptualization; investigation; methodology; visualization. **Fouz M. Omar:** Conceptualization; investigation; methodology; visualization.

ENDNOTES

[a] Theoretical μ_g using *Hyperchem* 7.52 at semiempirical level

[b] Experimental μ_g values calculated using Lippert–Mataga and Bakhshiev.[60]

ᶜ Experimental μ_g values calculated using Kawski–Chamma–Viallet correlation.[61]

ᵈ Calculated from Reichardt correlation.[65]

DATA AVAILABILITY STATEMENT

The data that support the findings of this study are openly available from the corresponding author upon reasonable request. Additional supporting information section at the end of this article.

ORCID

Fatma Samy https://orcid.org/0000-0002-9455-9133
Ali Taha https://orcid.org/0000-0001-6950-3843
Fouz M. Omar https://orcid.org/0000-0001-5933-2892

REFERENCES

[1] a) M. Shebl, S. M. E. Khalil, M. A. A. Kishk, D. M. EL-Mekkawi, M. Saif, *Appl. Organomet. Chem.* **2019**, *33*, e5147; b) J. Song, F. Zhang, Q. Hu, W. Jiang, D. Li, B. Zhang, *Chem. Cat. Chem.* **2021**, *13*, 924.

[2] a) A. Taha, A. A. M. Farag, O. M. I. Adly, N. Roushdy, M. Shebl, H. M. Ahmed, *J. Molec. Struct.* **2017**, *1139*, 31; b) D. Cappello, R. R. Maar, V. N. Staroverov, J. B. Gilroy, *Chem. – Eur. J.* **2020**, *26*, 522.

[3] a) M. M. E. Shakdofa, M. H. Shtaiwi, N. Morsy, T. M. A. Abdel-rassel, *Main Group Chem.* **2014**, *13*, 187; b) F. Samy, A. Taha, H. S. Seleem, A. A. T. Ramadan, *Egypt. J. Chem.* **2020**, *63*, 4243; c) B. Shao, I. Aprahamian, *Chem. Photo. Chem.* **2019**, *3*, 361.

[4] a) A. Taha, A. A. M. Farag, O. M. I. Adly, N. Roushdy, M. Shebl, H. M. Ahmed, *J. Molec. Struct.* **2017**, *1142*, 66; b) T. Malinauskas, I. Vilionskiene, J. V. Grazulevicius, V. Getautis, J. A. Reina, J. Sidaravicius, *Polym. Int.* **2008**, *57*, 1159.

[5] a) S. Aslkhademi, N. Noshiranzadeh, M. S. Sadjadi, K. Mehrani, N. Farhadyar, *Polyhedron* **2019**, *160*, 115; b) Y. A. Tyula, A. Zabardasti, H. Goudarziafshar, M. Kucerakova, M. Dusek, *Appl. Organomet. Chem.* **2018**, *32*, e4141.

[6] a) S. S. Firmino, S. C. André, Z. Hastenreiter, V. K. Campos, J. A. Lessa, *Inorg. Chim. Acta* **2019**, *497*, 119079; b) M. Abd-Elzaher, A. A. Labib, H. A. Mousa, S. A. Moustafa, M. M. Abdallah, *Research Chem. Intermediates* **2014**, *40*, 1923; c) M. Yousefi, T. Sedaghat, J. Simpson, M. Shafiei, *Appl. Organomet. Chem.* **2019**, *33*, e5137.

[7] a) A. D. M. Mohamad, M. J. A. Abualreish, A. M. Abu-Dief, *J. Molec. Liquids* **2019**, *290*, 111162; b) I. Babahan, A. Özmen, M. Aksel, M. D. Bilgin, R. Gumusada, M. E. Gunay, F. Eyduran, *Appl. Organomet. Chem.* **2020**, *34*, e5632.

[8] R. P. Bakale, G. N. Naik, C. V. Mangannavar, I. S. Muchchandi, I. N. Shcherbakov, C. Frampton, K. B. Gudasi, *Eur. J. Med. Chem.* **2014**, *73*, 38.

[9] G. S. Hegde, S. P. Netalkar, V. K. Revankar, *Appl. Organomet. Chem.* **2019**, *33*, e4840.

[10] E. Pahonţu, D. C. Ilieş, S. Shova, C. Oprean, V. Păunescu, O. T. Olaru, F. Ş. Rădulescu, A. Gulea, T. Roşu, D. Drăgănescu, *Molecules* **2017**, *22*, 650.

[11] a) F. Samy, M. Shebl, *Appl. Organomet. Chem.* **2020**, *34*, e5502; b) M. Shebl, *J. Mol. Struct.* **2017**, *1128*, 79; c) H. M. A. Abumelha, J. Heterocyclic, *Chem* **2018**, *55*, 1738.

[12] a) M. Mohanraj, G. Ayyannan, G. Raja, C. Jayabalakrishnan, *J. Coord. Chem.* **2016**, *69*, 3545; b) G. A. A. Al-Hazmi, K. S. Abou-Melha, N. M. El-Metwaly, I. Althagafi, F. Shaaban, M. G. Elghalban, M. M. El-Gamil, *Appl. Organomet. Chem.* **2020**, *34*, e5408.

[13] E. Jayanthi, M. Anusuya, N. S. P. Bhuvanesh, K. A. Khalil, N. Dharmaraj, *J. Coord. Chem.* **2015**, *68*, 3551.

[14] S. Um, Y. Kang, J. Lee, *Dyes Pigm.* **2007**, *75*, 681.

[15] F. León, P. Elizalde, P. Prieto, A. Sánchez-Migallón, A. M. Rodríguez, A. de la Hoz, *Dyes Pigm.* **2016**, *131*, 307.

[16] J. R. Ramírez, A. Ruiz-Carretero, M. A. Herrero, A. Sánchez-Migallón, A. de la Hoz, *Dyes Pigm.* **2016**, *124*, 203.

[17] M. Dinari, F. Gharahi, P. Asadi, *J. Molec. Struct.* **2018**, *1156*, 43.

[18] M. Shebl, M. A. El-ghamry, S. M. E. Khalil, M. A. A. Kishk, *Spectrochim. Acta A* **2014**, *126*, 232.

[19] S. Cascioferro, B. Parrino, V. Spanò, A. Carbone, A. Montalbano, P. Barraja, P. Diana, G. Cirrincione, *Eur. J. Med. Chem.* **2017**, *142*, 523.

[20] S. Cascioferro, B. Parrino, V. Spanò, A. Carbone, A. Montalbano, P. Barraja, P. Diana, G. Cirrincione, *Eur. J. Med. Chem.* **2017**, *142*, 328.

[21] S. Kumar, V. C. Rao, R. C. Rastogi, *Spectrochim. Acta A* **2001**, *57*, 41.

[22] N. Sharma, S. K. Jain, R. C. Rastogi, *Spectrochim. Acta A* **2007**, *66*, 171.

[23] M. K. Saroj, N. Sharma, R. C. Rastogi, *Fluoresc.* **2011**, *21*, 2213.

[24] N. G. Bakhshiev, *Opt. Spectrosk.* **1961**, *10*, 717.

[25] Y. Ooshika, *J. Phys. Soc. Jpn.* **1954**, *9*, 594.

[26] E. G. McRae, *J. Phys. Chem.* **1957**, *61*, 562.

[27] L. Bilot, A. Kawski, *Z. Natursorsch.* **1962**, *17a*, 621.

[28] E. Lippert, *Phys. Chem.* **1957**, *61*, 962.

[29] N. Mataga, Y. Kaifu, M. Koizumi, *Bull. Chem. Soc. Jpn.* **1956**, *29*, 465.

[30] F. Samy, F. M. Omer, *J. Mol. Struct.* **2020**, *1222*, 128910.

[31] F. Samy, A. Taha, *Egypt. J. Chem.* **2018**, *61*, 731.

[32] F. Samy, A. A. T. Ramadan, A. Taha, H. S. Seleem, *Asian J. Chem.* **2016**, *28*, 2650.

[33] H. S. Seleem, A. A. T. Ramadan, A. Taha, F. Samy, *Res. J. Chem. Sci.* **2011**, *1*, 109.

[34] M. M. Mashaly, H. A. Bayoumi, A. Taha, *Chem. Papers* **1999**, *53*, 299.

[35] A. Taha, *Synth. React. Inorg. Met.-Org. Chem.* **2001**, *31*, 205.

[36] A. Taha, B. El-Shetary, W. Linert, *Monatsh. Chem.* **1993**, *124*, 135.

[37] A. I. Vogel, *A Textbook of Quantitative Inorganic Analysis*, 4th ed., Longman, London **1987**.

[38] P. W. Selwood, *Magnetochemistry*, Interscience, New York **1956**.

[39] N. Dharmaraj, P. Viswanathamurthi, K. Natarajan, *Transition Met. Chem.* **2001**, *26*, 105.

[40] T. Mosmann, *J. Immunol. Methods* **1983**, *65*, 55.

[41] S. M. Gomha, S. M. Riyadh, E. A. Mahmmoud, M. M. Elaasser, *Heterocycles* **2015**, *91*, 1227.

[42] a) A. M. Clark, P. Labute, *J. Chem. Inf. Model.* **2007**, *47*, 1933; b) A. A. Fadda, E. Abdel-Latif, A. Fekri, A. R. Mostafa, J. Heterocyclic, *Chem* **2019**, *56*, 804.

[43] https://www.rcsb.org/

[44] Hyperchem version 7.5. Hypercube Inc.; **2003**.

[45] M. J. Frisch, G. W. Trucks, H. B. Schlegel, G. E. Scuseria, M. A. Robb, J. R. Cheeseman, G. Scalmani, V. Barone, B. Mennucci, G. A. Petersson, H. Nakatsuji, M. Caricato, X. Li, H. P. Hratchian, A. F. Izmaylov, J. Bloino, G. Zheng, J. L. Sonnenberg, M. Hada, M. Ehara, K. Toyota, R. Fukuda, J. Hasegawa, M. Ishida, T. Nakajima, Y. Honda, O. Kitao, F. Ogliaro, M. Bearpark, J. J. Heyd, E. Brothers, K. N. Kudin, V. N. Staroverov, R. Kobayashi, J. Normand, K. Raghavachari, A. Rendell, J. C. Burant, S. S. Iyengar, J. Tomasi, M. Cossi, N. Rega, J. M. Millam, M. Klene, J. E. Knox, J. B. Cross, V. Bakken, C. Adamo, J. Jaramillo, R. Gomperts, R. E. Stratmann, O. Yazyev, A. J. Austin, R. Cammi, C. Pomelli, J. W. Ochterski, R. L. Martin, K. Morokuma, V. G. Zakrzewski, G. A. Voth, P. Salvador, J. J. Dannenberg, S. Dapprich, A. D. Daniels, O. Farkas, J. B. Foresman, J. V. Ortiz, J. Cioslowski, D. J. Fox, *Gaussian 09*, Revision A. 1. Gaussian Inc., Wallingford, CT, USA **2009**.

[46] a) Q. Kang, L. Li, L. Wang, Y. Zhang, W. Dong, *Appl. Organomet.Chem.* **2019**, *33*, e5013; b) H. F. El-Shafiy, M. Shebl, *J. Mol. Struct.* **2019**, *1194*, 187; c) P. Sukanya, C. V. R. Reddy, *Appl. Organomet.Chem.* **2018**, *32*, e4526; d) H. F. El-Shafiy, M. Shebl, *J. Mol. Struct.* **2018**, *1156*, 403.

[47] a) W. Su, Y. Li, J. Xiao, Y. Zhang, P. Li, *Appl. Organomet. Chem.* **2018**, *32*, e4420; b) M. Shebl, O. M. I. Adly, E. M. Abdelrhman, B. A. El-Shetary, *J. Mol. Struct.* **2017**, *1145*, 329; c) M. Shebl, M. Saif, A. I. Nabeel, R. Shokry, *J. Mol. Struct.* **2016**, *1118*, 335.

[48] P. Naveen, B. V. Pandiyan, D. Anu, F. Dallemer, P. Kolandaivel, R. Prabhakaran, *Appl. Organomet.Chem.* **2020**, *34*, e5605.

[49] E. A. El-Samanody, S. A. AbouEl-Enein, E. M. Emara, *Appl. Organomet.Chem.* **2018**, *32*, e4262.

[50] A. K. El-Sawaf, Y. K. Abdel-Monem, M. A. Azzam, *Appl. Organomet.Chem.* **2020**, *34*, e5729.

[51] a) R. Fouad, M. Saif, *J. Molec. Struct.* **2020**, *1217*, 128472; b) H. F. El-Shafiy, *J. Mol. Struct.* **2018**, *1166*, 348.

[52] a) O. A. El-Gammal, A. S. Fouda, D. M. Nabih, *J. Molec. Struct.* **2020**, *1204*, 127495; b) M. Shebl, *J. Coord. Chem.* **2016**, *69*, 199.

[53] a) O. A. El-Gammal, A. F. Al-Hossainy, S. A. El-Brashy, *J. Mol. Struct.* **2018**, *1165*, 177; b) M. Shebl, O. M. I. Adly, A. Taha, N. N. Elabd, *J. Mol. Struct.* **2017**, *1147*, 438.

[54] a) H. S. Seleem, A. A. T. Ramadan, A. Taha, M. F. Eid, F. Samy, *Spectrochim. Acta A* **2011**, *78*, 1097; b) M. Shebl, S. M. E. Khalil, F. S. Al-Gohani, *J. Mol. Struct.* **2010**, *980*, 78.

[55] a) O. A. El-Gammal, M. Gaber, S. A. Mandour, *Appl. Organomet. Chem.* **2020**, *34*, e5699; b) H. S. Seleem, A. A. Emara, M. Shebl, *J. Coord. Chem.* **2005**, *58*(12), 1003.

[56] F. Samy, H. S. Seleem, A. Taha, M. Shebl, F. Hanfy, *Egypt. J. Chem.* **2019**, *62*(4), 691.

[57] S. M. E. Khalil, M. Shebl, F. S. Al-Gohani, *Acta Chim. Slov.* **2010**, *57*, 716.

[58] M. Shebl, *Spectrochim. Acta A* **2009**, *73*, 313.

[59] H. S. Seleem, B. A. El-Shetary, M. Shebl, *Heteroatom. Chem.* **2007**, *18*, 100.

[60] M. Shebl, H. S. Seleem, B. A. El-Shetary, *Spectrochim. Acta A* **2010**, *75*, 428.

[61] H. S. Seleem, B. A. El-Shetary, S. M. E. Khalil, M. Mostafa, M. Shebl, *J. Coord. Chem.* **2005**, *58*, 479.

[62] a) H. Katouah, A. M. Hameed, A. Alharbi, F. Alkhatib, R. Shah, S. Alzahrani, R. Zaky, N. M. El-Metwaly, *Chem. Select* **2020**, *5*, 10256; b) M. Shebl, S. M. E. Khalil, *Monatsh. Chem.* **2015**, *146*, 15; c) E. A. El-Samanody, M. W. Polis, E. M. Emara, *J. Mol. Struct.* **2017**, *1144*, 300; d) Y. K. Abdel-Monem, S. A. Abouel-Enein, *J. Therm. Anal. Calorim.* **2017**, *130*, 2257; e) E. A. El-Samanody, S. M. Emam, E. M. Emara, *J. Mol. Struct.* **2017**, *1146*, 868.

[63] W. J. Geary, *Coor. Chem. Rev.* **1971**, *7*, 81.

[64] a) O. A. El-Gammal, S. A. El-Brashy, G. M. Abu El-Reash, *Appl. Organomet.Chem.* **2020**, *34*, e5456; b) S. M. E. Khalil, H. S. Seleem, B. A. El-Shetary, M. Shebl, *J. Coord. Chem.* **2002**, *55*, 883.

[65] O. M. I. Adly, M. Shebl, H. F. El-Shafiy, S. M. E. Khalil, A. Taha, M. A. N. Mahdi, *J. Molec. Struct.* **2017**, *1150*, 507.

[66] M. Shebl, S. M. E. Khalil, S. A. Ahmed, H. A. A. Medien, *J. Mol. Struct.* **2010**, *980*, 39.

[67] a) O. A. El-Gammal, G. M. Abu El-Reash, R. A. Bedier, *Appl. Organomet.Chem.* **2019**, *33*, e5141; b) M. Shebl, *Spectrochim. Acta A* **2008**, *70*, 850; c) S. A. AbouEl-Enein, S. M. Emam, M. W. Polis, E. M. Emara, *J. Molec. Struct.* **2015**, *1099*, 567.

[68] M. Shebl, O. M. I. Adly, M. Shebl, H. F. El-Shafiy, S. M. E. Khalil, A. Taha, M. A. N. Mahdi, *J. Molec. Struct.* **2017**, *1134*, 649.

[69] a) E. S. Mousa, W. H. Mahmoud, *Appl. Organomet.Chem.* **2019**, *33*, e4844; b) M. Shebl, *J. Coord. Chem.* **2009**, *62*, 3217.

[70] M. Shebl, *Spectrochim. Acta A* **2014**, *117*, 127.

[71] K. Shalabi, O. A. El-Gammal, Y. M. Abdallah, *Colloids and Surfaces A* **2021**, *609*, 125653.

[72] Y. K. Abdel-Monem, S. A. Abouel-Enein, S. M. El-Seady, *J. Molec. Struct.* **2018**, *1152*, 115.

[73] S. M. Emam, S. A. AbouEl-Enein, E. M. Emara, *J. Therm. Anal. Calorim.* **2017**, *127*, 1611.

[74] a) A. A. A. Emara, M. A. Tawab, M. A. El-ghamry, M. Z. Elsabee, *Carbohydr. Polym.* **2011**, *83*, 192; b) M. Shebl, M. A. Ibrahim, S. M. E. Khalil, S. L. Stefan, H. Habib, *Spectrochim. Acta A* **2013**, *115*, 399.

[75] M. Shebl, S. M. E. Khalil, A. Taha, M. A. N. Mahdi, *Spectrochim. Acta A* **2013**, *113*, 356.

[76] A. Taha, *Spectrochim. Acta A* **2003**, *59*, 1373.

[77] J. R. Anacona, K. Ruiz, M. Loroño, F. Celis, *Appl. Organomet. Chem.* **2019**, *33*, e4744.

[78] M. Shebl, S. M. E. Khalil, A. Taha, M. A. N. Mahdi, *J. Mol. Struct.* **2012**, *1027*, 140.

[79] O. M. I. Adly, A. Taha, S. A. Fahmy, *J. Mol. Struct.* **2019**, *1186*, 362.

[80] a) O. M. I. Adly, A. Taha, M. Ahmed, S. A. Fahmy, *Appl. Organomet. Chem.* **2020**, *34*, e5763; b) W. Spiller, H. Kliesch, D. W€ohrle, S. Hackbarth, B. Roder, G. Schnurpfeil, *J. Porphyrins Phthalocyanines* **1998**, *2*, 145.

[81] U. S. Raikar, C. G. Renuka, Y. F. Nadaf, B. G. Mulimani, A. M. Karguppikar, M. K. Soudagar, Spectrochim, *Acta A* **2006**, *65*, 673.

[82] A. Kawski, in *Progress in Photochemistry and Photophysics*, (Ed: J. F. Rabek), CRC Press, Boca Raton, USA **1992** 5,1.

[83] E. Lippert, *Z. Naturforsch* **1955**, *10*, 541.

[84] N. Mataga, Y. Kaifu, M. Koizumi, *Bull. Chem. Soc. Jpn.* **1945**, *29*, 465.

[85] N. G. Bakhshiev, *Opt. Spektrosk.* **1964**, *16*, 821.

[86] K. Dhahagani, S. M. Kumar, G. Chakkaravarthi, K. Antitha, J. Rajesh, A. Ramu, G. Rajagopal, *Spectrochim. Acta A* **2014**, *117*, 87.

[87] M. Borowiak, A. N. Garratt, T. Wustefeld, M. Strehle, C. Trautwein, C. Birchmeier, *Proc. Natl. Acad. Sci. U. S. A.* **2004**, *101*, 10608.

[88] T. A. Yousef, G. M. Abu El-Reash, O. A. El-Gammal, S. F. Ahmed, *Polyhedron* **2014**, *81*, 749.

[89] V. Gutmanns, *The Donor-Acceptor Approach to Molecular Interaction*, Blenny Press, New York and London **1978**.

[90] F. M. Omar, F. Samy, *J. Mol. Struct.* **2021**, *1242*, 130744.

SUPPORTING INFORMATION

Additional supporting information may be found online in the Supporting Information section at the end of this article.